Solid Freeform Fabrication 2017: Proceedings of the 28th Annual International Solid Freeform Fabrication Symposium – An Additive Manufacturing Conference
Reviewed Paper

CONSTRUCTION OF METALLIC GLASS STRUCTURES BY LASER-FOIL-PRINTING TECHNOLOGY

Yiyu Shen, Yingqi Li, and Hai-Lung Tsai

Department of Mechanical and Aerospace Engineering, Missouri University of Science and Technology, Rolla, MO 65409

Abstract

Metallic glasses (MGs) have superior mechanical properties such as high tensile strength, hardness, and corrosion resistance, as compared to crystalline metals. Although newly developed MGs have significantly reduced critical cooling rates down to 10 K/s, products of MGs are still limited to simple geometries such as foils/plates or rods with thin section-thickness which is mainly caused by the decrease of thermal conductivities of the new MGs. Recently, we developed a new Laser-foil-printing (LFP) additive manufacturing technology which welds foils, layer by layer, to construct desired 3D structures. With the LFP and Zr-based amorphous foils, 3D, large amorphous structures with complex geometry have been successfully manufactured. To better understand the evolution of crystalline phase, we integrate the finite element based heat transfer model and classic nucleation theory (CNT) based crystal nucleation/growth model. The model was used to demonstrate the evolution of crystal phase as a function of time during laser welding at different locations including the fusion zone (FZ) and heat-affected zone (HAZ). The model is also compared favorably with the experiment results. The reported susceptibility to crystallization in HAZ were discussed and explained.

Introduction

Metallic glasses (MGs) or amorphous alloys can be produced by rapid quenching and solidification of molten metals to bypass crystallization. Atoms in amorphous metals exist in a random/disordered manner much like atoms in the liquid phase. Compared to traditional crystalline metals, MGs have superior properties such as high tensile strength, hardness, wear resistance, and corrosion resistance [1−5]. These properties are inherited from randomness/disorder of atoms in the MG which is different from crystallized metals in which periodic arrays of atoms, called crystal lattices, are arranged in an organized, structured manner. In a crystalline metal, however, mainly due to multi-directional slow cooling and solidification, defects/dislocations/segregations always exist between grains/crystals (grain boundaries or interfaces) which are the “weak spots” and could initiate “cracks” when subjecting to external loading, propagating and eventually leading to the failure of the entire structure. Hence, tensile strength, for example, for a “normal” crystalline metal can only be a fraction of otherwise “perfect” crystal lattices of the same metal composition.

The main challenge of producing large metallic glass part/structure is that a certain high cooling rate must be reached otherwise the alloy would been crystallized before it cools down to room temperature. This is named as the critical cooling rate (R_c). Once crystallized, the unique mechanical properties could be lost. Limited by the manufacturing method, this critical cooling rate also limits the size of MG part to be produced. One example is the casting method, which is currently the most widely used method for produce MG parts in this area. During casting the

material who is away from the surface cools less fast compare to that close to the outer surface. Thus, a defined critical cooling rate is equivalent of an upper limit of casting thickness. Additive manufacturing, however, build up the designed part layer by layer. The success application of AM technology on MG structures will separate the cooling process into every individual layer. As a result, once the feasibility of AM for metallic glass is proved, the limitation of dimension in manufacturing metallic glass product can be broken through. Unfortunately, to date no successful result has been published. Given that the outstanding mechanical properties and high application potential of MG, fundamental research is required to address the significant technological challenges and bridge the capability in AM of MG structures.

In laser material processing, as a large amount of energy is tightly focused onto a very small area, the heating rate (R_h) and R_c of the processed part are very high ($10^4 \sim 10^5$ K/s) [6]. This makes laser-based AM technologies naturally a promising method in building large MG parts [7]. Recently, Sun [8] studied the microstructure evolution of Vitreloy 106a MGs processed by LENS technology. He pointed out that the crystallization phenomenon in the heat-effected zone (HAZ) took place even at a R_c of 10^4 K/s due to complex thermal history. Hence, preventing crystallization in the HAZ is the main challenge rather than in the melting zone. Zhang et al. [9] have found a similar phenomenon in powder-based AM process. Therefore, it is vital important to understand the crystallization mechanism behind the laser-MG interaction. This is different from the posted researches on regular crystallization of MGs[11-13].

In this paper, we first demonstrate the use of developed laser foil printing (LFP) technology to weld amorphous foils, layer-by-layer, via laser to construct 3D MG parts. Then, the evolution of crystallization phase during the laser welding on Zr- based MG is studied. A finite element based heat transfer model is applied to obtain the temperature history in the HAZ. After that, classic nucleation theory based nucleation/growth model is applied to calculate the evolution of crystalline phase.

The laser foil printing (LFP) technology

Details of the LFP technology can be found in Ref. [14]. However, in order to better demonstrate how a part is manufactured, which will affect the formation of crystalline, and also to discuss the effect of process parameters, the method, system, and procedure for the LFP technology are briefly described below. A schematic of the LFP process is given in Fig. 1. The LFP process is mainly realized by two alternative processes: foil-welding by a continuous wave (CW) fiber laser and foil-cutting by a pulsed UV laser. A fresh foil is first loaded on the substrate and then fixed by spot-welding, the program controls the scanner to scan a specified pattern path of the CW laser beam on the foil to weld the foil to the substrate. Depending upon the desired R_c for different amorphous alloys, welding can be accomplished via line-welding or a matrix of spot-welding. The welding path/pattern should be designed (which depends on the geometry of the part) to achieve symmetrical welding in order to minimize possible thermal stress/part distortion, and at the maximum separations in time and in space between two consecutive weldings to avoid heat accumulation and achieve high cool rates. For example, for a spot-welding at location A, the next spot-welding at location B should be as far as possible from A. After the welding process is done, an X-Y motion stage shifts the part to the location under the UV laser beam. Then, the program controls the X-Y motion stage and the UV laser to cut the welded foil along the outer and/or inner

circumferences of the part. After the laser cutting is completed, the redundant foil is removed and another fresh foil is placed and fixed on the top of the sample. The aforementioned entire process can be fully automatic. This procedure is repeated until the whole desired 3D part is built. Note, in the two alternative processes, laser welding can be done ahead of laser cutting or vice versa.

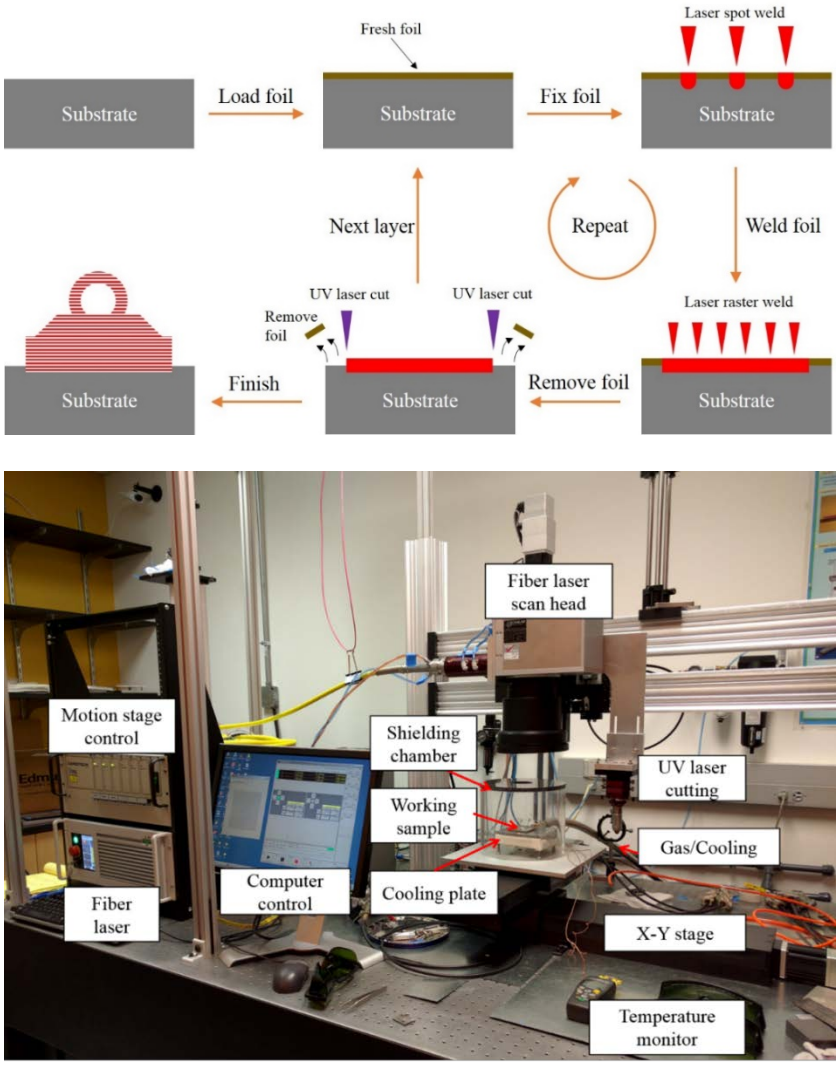

Fig. 1. Schematic of the LFP process and the LFP system setups at the Laser-Based Manufacturing Lab, Missouri S&T.

Figure 1 also shows the LFP setup developed at the Laser-Based Manufacturing Lab, Missouri S&T. The welding laser is an IPG YLR-1000 CW (continuous wave) fiber laser with a wavelength of 1070 nm and a maximum output power of 1000 W. The cutting laser is a Coherent AVIA-355X laser with 355 nm UV wavelength, Q-switched, 30 ns pulse duration and 10 W maximum power. The UV laser, not shown in the figure, is located in another room. The welding laser beam passes through an optical fiber, enters a collimator to become an expanded parallel beam, then enters the scanner (hurrySCAN25, SCANLAB), and finally is focused on the foil through an F-theta lens with an effective focal length of 33 cm. The cutting UV laser beam passes through several turning mirrors and is focused by a focusing lens with a 10-cm focal length. A cooling chamber with a heat exchanger plate at the bottom by passing through liquid nitrogen or liquid argon is designed

to achieve rapid cooling while the amorphous structure is being manufactured. The collimator and scanner for the fiber laser, and the focusing lens for the UV laser are mounted on a Z (vertical) motion stage. The foil is first positioned and fixed onto the substrate via spot-welding using a mold plate with predetermined hole-pattern, and the entire structure is placed on an X-Y (horizontal) motion stage (Aerotech). The two lasers, scanner and three-axis motion stage are integrated through control programs to a computer.

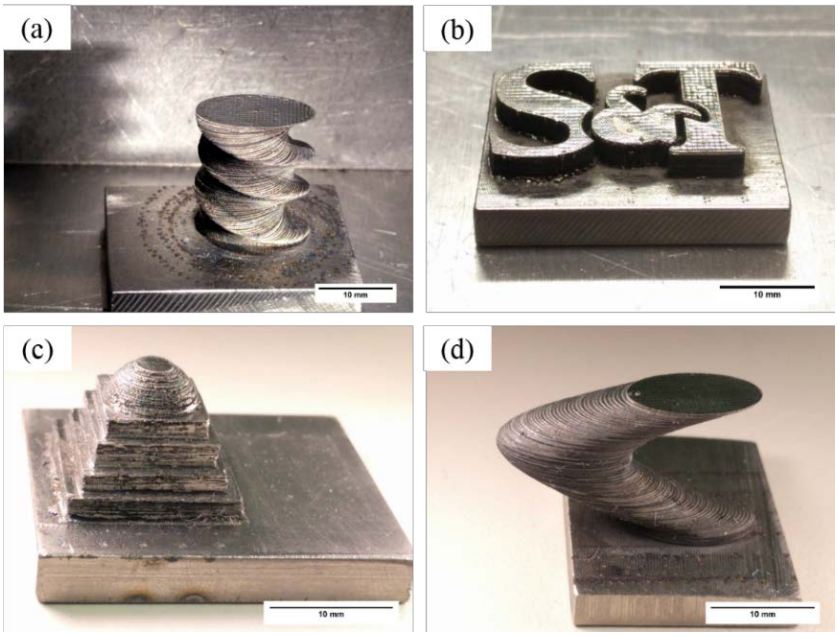

Fig. 2. As-fabricated amorphous 3D parts by LFP.

Figure 2 shows a few 3D MG parts printed by LFP from our previous publication [24]. Fig. 2(a) is a side view of a "metal fusilli pasta" part created by a continuous rotation of an ellipse pattern. Fig. 2(b) shows a 3-mm-thick amorphous "S&T" logo of the Missouri University of Science and Technology. A 5-stage 3D table, includes 4-square stages and a semi-spherical cover on the top is shown in Fig. 2(c). The overall height of the part was measured to be 11.3 mm. Fig. 2(d) is a slipped cylinder with overall displacement of 13 mm. All 4 samples were examined to be fully amorphous by XRD.

Experiment and Results

Cast Zr-based MG alloy, LM105 ($Zr_{52.5}Ti_5Al_{10}Ni_{14.6}Cu_{17.9}$ (at. %)) was used in this study. The cast Zr-based MG alloy, as samples, with a thickness of 0.75 mm, were machined into several specimen, each with 10 mm in length and width. All sample surfaces were polished with 800-grit SiC paper right before the experiment. Laser welding is applied (bead on plate) on the prepared samples. The laser used in this study is a continuous-wave (CW) fiber laser (model YLR-1000, IPG Photonic Corp.) with output wavelength of 1070 μm. The laser beam diameter *D* on the focal plane is 430 μm. The motion of the laser beam is controlled by a scanner (hurrySCAN III, SCANLAB) with the maximum scan speed of 2000 mm/s at the focal plane. All experiments were conducted in an argon shielded chamber. To determine suitable processing parameters, the laser power (*P*) was set to 100 W, while the laser scan speed (*v*) was varied from 10 mm/s to 500 mm/s.

As the main work of this study is to melt the surface of an MG sample at a depth of less than 200 μm, the laser power was selected at a relatively low value to avoid possible formation of keyholes during welding. The laser processed samples were cross-sectioned, polished and then etched by a solution of 100 ml H_2O, 2 ml H_2O_2 and 0.1 ml HF for 10 seconds and then examined by an optical microscope (OM) and scanning electron microscope (SEM, Helios S600).

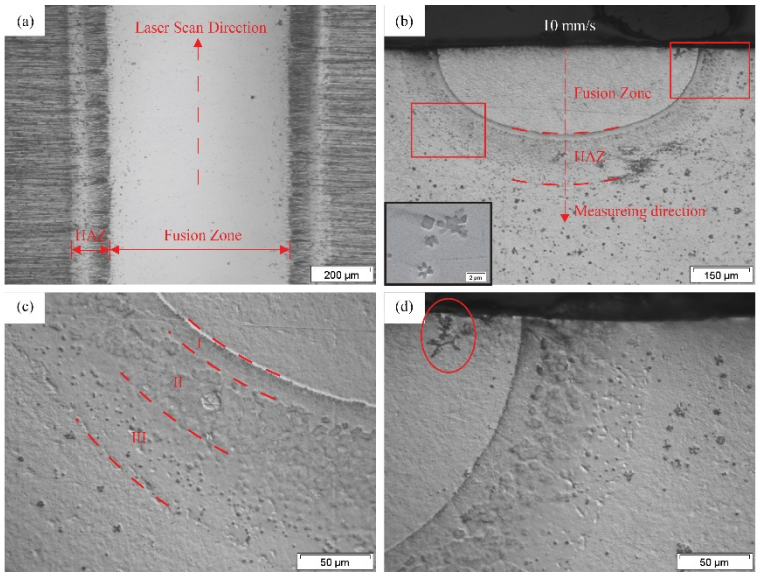

Fig. 3. Top and cross-sectional views of laser treated MG at a laser scan speed of 10 mm/s.

Figures 3 shows the top and cross-sectional views of the laser treated surfaces at laser power P = 100 W and scan speed v = 10 mm/s. As shown in Fig. 3(a), a 700 μm wide FZ was created on the top surface with ~100 μm wide HAZ on each of its two sides. From the corresponding cross section image in Fig. 3(b), along the vertical centerline the depth of FZ was measured as 235 μm. The thickness of the HAZ reaches a maximum of approximately 140 μm directly below the FZ. The micro-crystalline (MC) phases can be clearly seen pre-existed embedded in the amorphous matrix shown as the dark-spots in the image. A back scattering SEM image (Helios, ETD detector, BSE mode) for an enlarged view of typical MC crystals is given in inset (bottom left of Fig. 3(b)). For the as cast LM105, the volume fraction (VF) of MC crystalline was measured as 2.14%. The volume fraction of crystalline phase were estimated from the OM image of the etched cross section surface with ImageJ software [20−23]. Two selected areas in HAZ in Fig. 3(b) are enlarged and shown in Figs. 3(c) and 1(d). In HAZ there are clearly three distinct regions, as shown in Fig. 3(c); region I, as marked, is next to the FZ. An obvious difference in color change between HAZ and FZ can be seen after etching. While in region I there are no obvious MC particles observed and its thickness is about 16.0 μm. In region II, however, spherical-like MC crystals are observed with an average diameter of 4.34 μm. Region II is about 64.4 μm thick. In region III, sub-size crystalline phases are clearly seen. The average diameter of the phase is about 1.34 μm and the thickness of region III is approximately 53.8 μm. (Note the thickness of HAZ slightly dependents on the direction. In order to keep consistent with further discussion, we choose the downward direction as shown in Fig.3 (b).)The distinct appearances of the three regions in HAZ is believed to be caused by different thermal histories experienced in each region during the laser processing. Materials in region I are most close to FZ, so they experienced temperatures close to melting. Based on Ref.

[17], the melting temperature of LM105 is 1085 K. Thus, region I may has reached to the temperature point beyond the maximum crystalline grow rate, resulting a relatively small crystal size. In region II, materials were rapidly heated to around 1000 K at which the crystal growth rate is about the maximum and, as a result, the size of crystalline phase is larger than those in other two regions. In region III, the materials reach the temperature at which the nucleation rate is high and near its maximum. Hence, dense but smaller crystalline phases are expected. To understand the aforementioned phenomena, detailed analysis and explanation are postponed to next section with the help of mathematical modeling.

In Fig. 3(d), a cluster of MC crystal is observed near the top-right corner of the FZ. The size of the cluster is about 40 μm in diameter, which is significantly larger than the pre-existed MC crystal. We believe the formation of this MC crystal in FZ is caused by the follow reasons. Amorphous phase has a higher energy status as compared with crystalline phase (denoted as Gibbs free energy, ΔG); hence, to be melted, the crystalline phase needs more thermal energy. Assuming the laser heat deposition rates are the same for crystalline phase and its nearby amorphous phase, the crystalline phase requires a longer time to get melted as compared to the nearby amorphous phase. In other words, crystalline phase may still stay in its solid status after nearby amorphous phase is melted. For a Gaussian-like beam profile, at the edge of the FZ (melt pool), the crystalline phase may not have enough laser energy to get fully melted as compared to its nearby amorphous phase or that in the center of the FZ. The un-melted MC phase acts like a pre-existed crystal, and the size of the crystalline phase may grow and becomes larger during the cooling process.

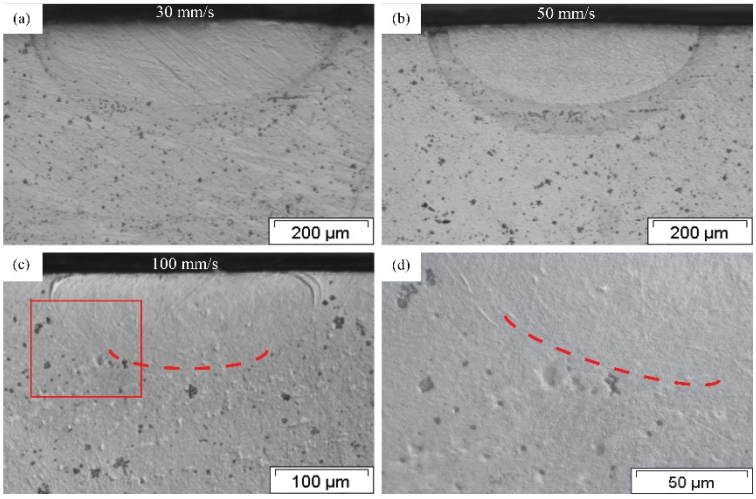

Fig. 4. Cross-section view of laser treated MG at laser scan speeds of 30 mm/s, 50 mm/s and 100 mm/s.

Figure 4 shows laser treated cross-sections at v = 30, 50 and 100 mm/s, respectively, for Figs. 4(a), 4(b) and 4(c). The size of FZ decreases with the increase of scan speed, as expected. Fig. 4(d) is an enlarged image for v = 100 mm/s, Fig. 2(c). The size of HAZ also decreases with the increase of v. The HAZ is no longer observable in Figs. 4(c) and 4(d). Further increase of the laser scan speed causes a dramatic decrease of the size of FZ and thus, there is no need for further increase of laser scan speed beyond 100 mm/s.

The crystallization process during laser-MG interaction is more complex than that during casting process. In the casting process, the temperature cools directly from above the melting temperature to below the glass transition temperature, which can be simplified to a value of critical cooling rate. While in the laser-MG interaction, the temperature first rises from room temperature to above melting and then followed by a rapid cooling back to below glass transition temperature. Thus the critical cooling rate may not be sufficiently applied in the laser-MG interaction case. To better understanding the crystallization evolution during laser-MG interaction process, we setup a coupled model combined with heat transfer and classic nucleation theory (CNT) in this study. The heat transfer model is used to estimate the temperature history at the selected point, while the CNT model is used to estimate the volume fraction evolution of crystalline phase in the amorphous matrix.

The heat transfer model and the related assumptions and validation have been discussed in our previous paper [24]. However, to facilitate the following discussion, the heat transfer model is briefly discussed. For heat conduction, the governing differential equation can be written as:

$$\frac{\partial}{\partial x}\left(k\frac{\partial T}{\partial x}\right)+\frac{\partial}{\partial y}\left(k\frac{\partial T}{\partial y}\right)+\frac{\partial}{\partial z}\left(k\frac{\partial T}{\partial z}\right)=\rho C_p\frac{\partial T}{\partial t} \quad (1)$$

where T denotes the temperature, t is the time, k is the thermal conductivity, ρ is the material density and C_p is the specific heat. The heat losses from the part's surfaces to the surroundings are assumed to be thermal radiation and heat convection, and they are:

$$-k\frac{\partial T}{\partial n}=\epsilon\sigma(T^4-T_\infty^4)+h(T-T_\infty) \quad (2)$$

where n is the normal direction to the surface which can be the x-, y- or z-direction, ϵ is the surface emissivity, σ is the Stefan-Boltzmann constant and h is the convective heat transfer coefficient. The laser power is assumed to be a Gaussian distribution at the top surface (z-plane) which is expressed as:

$$I_{laser}=\alpha\cdot\frac{2*P}{\pi r^2}\cdot e^{\frac{-2[(x-vt)^2+y^2]}{r^2}} \quad (3)$$

where I_{laser} represents the laser power density, α is the surface absorptivity, P is the laser power, r is the laser beam radius and v is the laser scan speed. The x-, y-, x-coordinate system was established at the center of the top surface for the plate with the dimensions of 10 mm by 10 mm by 0.75 mm. The calculated domain was: x (−5 mm, 5 mm), y (−5 mm, 5 mm), and z (0 mm, −0.75 mm). The laser scanned from (x = −5 mm, y = 0 mm, z = 0 mm) toward the positive x direction. From the heat transfer model, the temperature history at any location can be calculated.

For the nucleation model, the classic nucleation rate writes [25]:

$$I(T)=A\cdot D\cdot\exp(-\frac{\Delta G^*}{kT}) \quad (4)$$

where I is the nucleation rate, A is a constant, D is the effective diffusivity, k is the Boltzmann's constant, T denotes the absolute temperature and ΔG^* is the thermodynamic potential barrier of nucleation. ΔG^*obeys the following relation:

$$\Delta G^*=\frac{16\pi\sigma^3}{3\Delta G^2} \quad (5)$$

where σ denotes the interface energy between nucleus and melt, and ΔG is the difference of Gibbs free energy between the solid and liquid (amorphous) phase. The diffusion limited crystalline growth velocity U can be expressed by [25]:

$$U(T)=\frac{D}{a}[1-\exp(-\frac{\Delta G}{kT})] \quad (6)$$

where a is the average interatomic spacing. Considering diffusion limited crystal growth, the 3D time-dependent VF of crystallized phase $X(t)$ is [9,26]:

$$X(t) = 1 - \exp\left\{-\frac{4\pi}{3} \cdot \left[\int_0^t I(\tau)\left[\int_\tau^t U(t')dt'\right]^3 d\tau + N \cdot \left[\int_0^t U(t'')dt''\right]^3\right]\right\} \quad (7)$$

Note I and U each is a function of temperature T. As T is a function of time and location from the heat transfer model, I and U each is a function of time and location. N represents the pre-existed nucleus density (unit in m^{-3}) in the sample. It is reset to 0 when $T > T_m$ due to melting where T_m = 1085 K is used in this paper.

The aforementioned equations are numerically solved with the parameters determined below. The temperature dependent effective diffusivity, D, calculated from measured viscosity in Ref. [27] by Stork-Einstein relation [26]. The Gibbs free energy difference between undercooled liquid and corresponding crystal solid, ΔG, as a function of temperature given in Ref. [28] was used in the present study. The reported nose temperature of 860 K from Ref. [29] was used. By evaluating the maximum value of $I \times U^3$ which corresponds to the nose temperature in the TTT curve, σ can be determined as 0.076 J/m^2 [30]. Then, the constant, A, can be determined by running Eq. (7) with N = 0 at the nose temperature and examining the time of crystallization which matches the TTT curve [26,29]. The constant A was found to be 2.5×10^{33}. Finally N can be determined by running Eq. (7) using the thermal history in manufacturing from the liquid phase to room temperature. However, as it is difficult to know the exact thermal history during manufacturing; instead, we used the evaluated VF of the sample (2.14%) and predicted the equivalent averaged cooling rate during manufacturing which is about 50 K/s. Thus, the pre-existed nucleus density was determined by integrating the nucleation rate w.r.t. time, which is $N = 1 \times 10^{14}$ m^{-3}. For a selected location, by plugging the temperature history $T(t)$ obtained from the heat transfer model, Eq. (1), into Eqs. (4) and (6) to calculate $I(t)$ and $U(t)$, respectively, and, then, the VF of crystalline phase, $X(t)$, as a function of time was computed by Eq. (7). Hence, for the entire sample domain, the VF of crystalline phase can be obtained as a function of time and location.

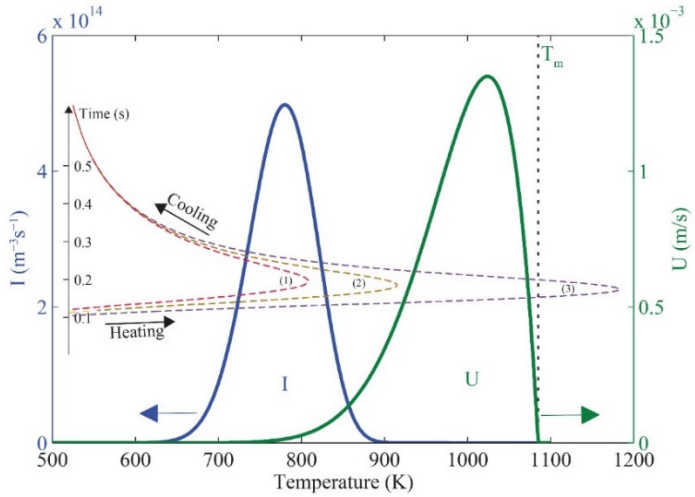

Fig. 5. Solid lines: The calculated nucleation rate ($I(T)$) and crystalline growth rate ($U(T)$) as a function of temperature. Dashed line: calculated temperature history of laser scan with P = 100 W and v = 10 mm/s at different locations. Curve (1): bottom of HAZ (region III in Fig. 1(d)), Curve (2): middle of HAZ (region II in Fig. 1(c)), and Curve (3): in FZ.

Figure 5 plots the calculated I and U as a function of temperature for LM105 alloy. It is seen the peak of nucleation rate occurs at the temperature of about 780 K. However, the maximum crystal growth rate occurs at about 1030 K, and then drops rapidly to 0 at the melting temperature T_m = 1085 K. Figure 5 also plots the calculated temperature histories for three points in the sample at laser power P = 100 W and scan speed v = 10 mm/s. The three dashed curves represent the heating and cooling histories for the points at (x = 0 mm, y = 0 mm, z = −0.35 mm), (0, 0, −0.3), and (0, 0, −0.18), respectively. For Curve (1) representing the heating and cooling for point (0, 0, −0.35), which is located in HAZ but far away from FZ (region III in Fig. 1(c)), it is heated to about 810 K by laser in 0.1 s and then followed by rapid cooling to below 500 K in around 0.5 s. The curve (point) experiences much nucleation while touches only a little bit of crystal growth, which implies that there would be high dense with relatively small crystalline phase generated. For the point (0, 0, −0.3) as presented in Curve (2) of Fig. 3 (region II in Fig. 1(c)), it reaches about 920 K. This is the temperature that U is high and one would expect larger sizes of crystalline phase to be observed here. For Curve (3), which is for the point (0, 0, −0.18) located in FZ, the temperature exceeds the melting temperature in around 0.05 s. It is reasonable to assume that all crystalline phases/amorphous/nuclei will be melted while melting occurs (see also in Fig. 6). In the cooling process, the liquid alloy first experiences the temperature range in which U is very high in the temperature range, 920 K ~ 1080 K. However, as it was free of nuclei in the newly solidified alloy, the growth of crystalline phase is not significant. Then, the alloy experiences the temperature range where nucleation is high, but the growth is low, leading to a certain amount of nuclei in the alloy after cooling to the room temperature. The aforementioned discussions explain and consistent with the results obtained from experiments as shown in Fig. 3 at different locations in the sample.

From Fig. 5, if an amorphous alloy is cooling down from its molten state, as there is no nucleation site even the cooling curve hit the crystal growth curve, $U(t)$, the volume fraction of crystalline phase, $X(t)$, is very minimum until it hit the nucleation curve $I(t)$ at which nucleation sites start to be generated. However, at this time the crystal growth rate decreases to small and, hence, the $X(t)$ is limited. The dependence of $X(t)$ is not very critical for cooling from the molten state, particularly during the manufacturing process (e.g., mold casting). However, if a solid amorphous alloy is heated from room temperature by, for example, a laser, then the location and its heating/cooling rates would be very critical for the $X(t)$. If a point is located in the HAZ, it would experience twice of passing through the $I(t)$ and $U(t)$ curves during its heating and cooling processes and, hence, the accumulated $X(t)$ is great. This explains the reports that why crystallization occurred in HAZ even the cooling rate is much higher than the critical cooling rate for amorphous phase [9−13]. Based on the aforementioned discussion, it is easy to understand that the pre-existed nucleus density, N, would have a significant effect on $X(t)$ in HAZ.

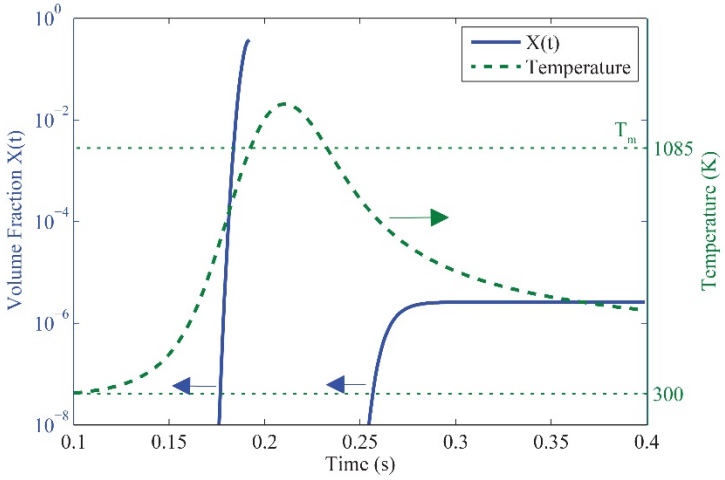

Fig. 6. Calculated the evolution of volume fraction of crystalline in FZ.

Figure 6 shows the calculated $X(t)$ in FZ for the same condition shown in Fig. 3(b) with laser power P = 100 W and scan speed v = 10 mm/s. The location studied is (0, 0, −0.18), also the same as Curve (3) in Fig. 5, which is in FZ (the calculated depth of fusion zone is 230 μm from the top surface). The dashed curve represents the temperature history from the heat transfer model. The "discontinue" solid curve in Fig. 4 represents the evolution of $X(t)$ as a function of time. The VF of crystalline increases rapidly upon heating to about 38% at t = 0.192 s. Then, melting starts and clears the crystalline/nuclei at t = 0.192 to 0.232 s. Upon cooling and starting at t = 0.232 s, $X(t)$ grows from 0 again and ends up with a near constant value of 2.6×10^{-6} at t = 0.4 s. The final residual nucleus density in the sample, N_{res}, is calculated as 2.23×10^{13} m^{-3} which is only 22% as compared to the initial nucleus density $N = 1\times10^{14}$ m^{-3}. Note, this number of residual nucleus density is equivalent to the pre-existed nucleus density for the later thermal circles.

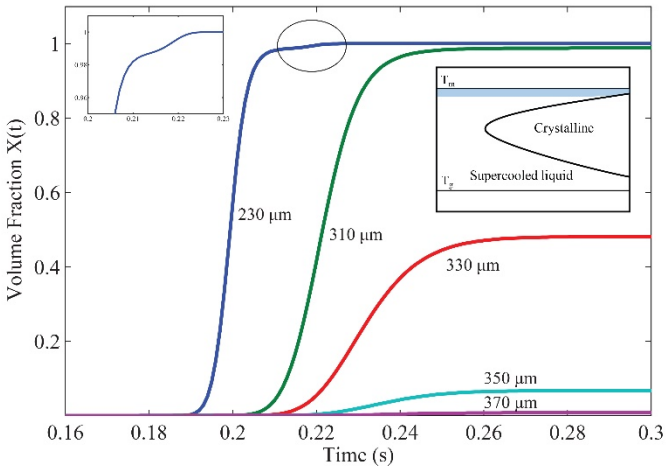

Fig. 7. Calculated the evolution of volume fraction of crystalline in HAZ at different depths.

Figure 7 plots the evolution of VF of crystalline $X(t)$ at different locations in HAZ shown in Fig. 1(b) with P = 100 W and v = 10 mm/s. Note in the experiment, the depth of FZ was measured

as 235 μm and followed by an about 140 μm thick of HAZ (also see Fig. 8). In the modeling, the depth of FZ was calculated as 230 μm. From Fig. 7, for a point in HAZ but just right below FZ (0, 0, −0.23), $X(t)$ grows to 100% rapidly. Unlike what happened in FZ, melting, which is able to reset the crystalline percentage to 0, the value of $X(t)$ at any location in HAZ increases and then reaches a steady-state constant value through the entire heating-cooling process. The VF of crystalline phase ends up with 98.82%, 48.14%, 6.74 %, and 0.76 % at the depth of 310 μm, 330 μm, 350 μm and 370 μm, respectively. It is considered to be undetectable (0.76 % < 2 %) at the 370 μm depth for *X(t)*. Thus, the calculated thickness of HAZ is around 135 μm (~365 μm – 230 μm), which is consistent with the experimental result, ~140 μm, as shown in Fig. 3(b).

The curve at the depth of 230 μm from t = 0.21 to t = 0.23 s, as shown in the enlarged inset on left-top, indicates a "dent" in the crystallization rate curve between t = 0.21 s and 0.22 s. This "retardation of crystallization" is in fact expected [31] and can be well explained with the help of Fig. 5. From Fig. 5, it can be seen that for temperatures below (but close to) T_m (e.g., 1035 K to T_m = 1085 K), *U(t)*, the crystal growth rate decreases rapidly from its maximum to almost 0. Hence, for a point in HAZ but next to FZ if its heating history is such that the maximum temperature is very close to the melting temperature (but not yet melted), the crystallization process freezes. The retardation of crystallization is also frequently observed from the well-known TTT curve of metallic glasses. As can be seen in the right inset image of Fig. 7, at temperatures just below T_m (the shaded area) the supercooled liquid can stay in its amorphous status for a long time because of the frozen of crystallization. Thus, to the position next to the fusion zone, the average crystalline size would expected to be smaller. Note, this phenomenon may be only observed under rapid heat/cooling to the sub melting temperature like in laser welding. Under a relatively slow heating/cooling, fully crystallization would be reached already before the temperature gets high enough [32]. An example is given in Fig. 8 where the final VF of crystalline is plotted as a function of depth from the surface, as shown in the inset, for laser scan speeds of 10 and 30 mm/s. The region on the left where VF = 0 represents the fusion zone. For v = 10 mm/s, the VF of crystalline reaches 100% at the depth of 223 μm, which is the start of HAZ just below the FZ. With the increase of depth, the VF of crystalline first keeps steady (100%) and then starts to drop at the depth about 280 μm to below 2% at the depth of 346 μm. If the criteria of fully amorphous is set to the final VF of crystalline < 2%, the thickness of HAZ is measured as 123 μm (346 μm minus 223 μm) under laser scan speed v = 10 mm/s. While for scan speed v = 30 mm/s, the final VF of crystalline is found to be about 43% right below FZ at the depth about 175 μm. It is noticed that the final VF of crystalline increases to about 50% at the depth about 182 μm and then drops back to 0 for higher depths, resulting in a 72 μm thick of HAZ (247 μm minus 175 μm). The maximum VFs of crystalline at other laser scan speeds are given in Fig. 8. As shown in Fig. 8, when the laser scan speed is about 17 mm/s or lower, the maximum VF of crystalline reaches 100%.

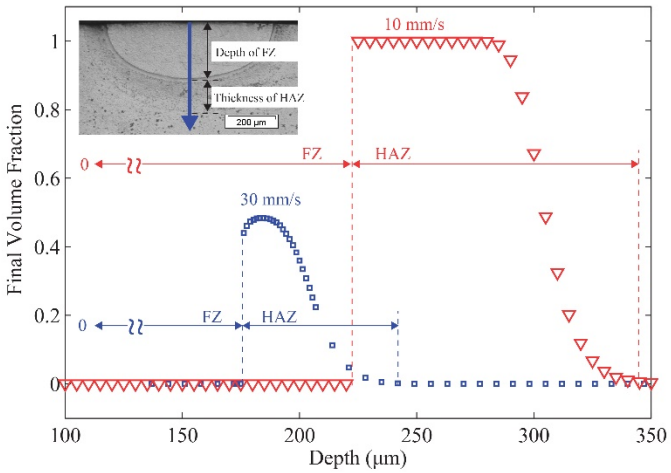

Fig. 8. Calculated final volume fraction of crystalline as a function of depth at different laser scan speeds.

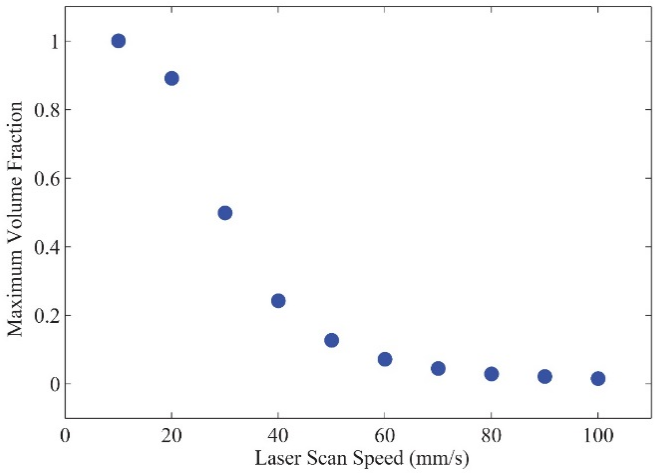

Fig. 9. Calculated maximum crystalline VF at different laser scan speeds.

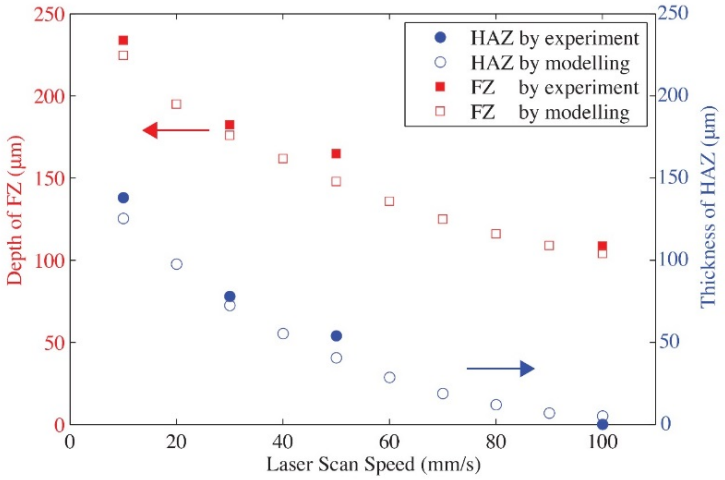

Fig. 10. Calculated and measured depth of fusion zone (FZ) and thickness of heat-affected zone (HAZ) as a function of laser scan speed at a fixed laser power (P =100 W).

The depth of FZ and the thickness of HAZ from experiments and modeling are shown in Fig. 8. For a fixed laser power P = 100 W, the scan speed v increases from 10 mm/s to 100 mm/s with an increment of 10 mm/s. The depth of FZ in the modeling were counted from the top surface to the depth at where T = 1085 K, the melting temperature. The thickness of HAZ was counted from the bottom of FZ to the location at where final crystalline VF goes below 2% (see the inset of Fig. 6). The experimental data were measured from the cross-section images presented before.

It can be seen from Fig. 10 that for relatively low scan speeds (10 mm/s and 20 mm/s), the HAZ is thicker than 100 μm. At the scan speed of 50 mm/s, the thickness of HAZ is calculated around 50 μm. Further increases of laser scan speed lowers the HAZ thickness to almost 0 at 90 or 100 mm/s of scan speeds. Similarly, the depth of FZ also decreases as the laser scan speed increases, as expected. The depth of FZ at P = 100 W and v = 100 mm/s is 105 μm, which is close to the experimental result, 110 μm, shown in Fig. 4(c). Since at this speed, no crystallized HAZ is observed and, hence, further increase of scan speed can only decrease the depth of FZ.

Conclusions

In this paper, evolution of the crystalline phase in HAZ during laser welding on Zr- based MG is studied. Using a model couples with heat transfer and classic nucleation theory, the crystallization during laser-MG interaction is accurately predicted. Based on the aforementioned discussion, we can draw the following conclusions: (1) In laser-MG interaction, the major challenge is to suppress the crystallization in HAZ. Increasing laser scan speed will reduce the size of crystallized HAZ. In the HAZ for low laser scan speed (10 mm/s), three distinct crystallized regions was observed. This is explained by the different temperature history induced different crystallization history. (2) Classic nucleation theory is successfully applied in describing the crystallization process of LM105 alloy. The modeled results marches well with the experiments conducted. This model can be used in future work to further studying the laser welding and laser-based additive manufacturing of metallic glasses.

Acknowledgements

The authors would like to acknowledge the financial support by the Intelligent Systems Center at Missouri S&T, the Department of Energy (Grant Number: DE-FE0012272) and the UM Fast Track Funding Program.

References

[1] W.L. Johnson, Bulk metallic glasses − a new engineering material, Current Opinion in Solid State and Materials Science 1 (3) (1996) 383-386. DOI http://dx.doi.org/10.1016/S1359-0286(96)80029-5.

[2] E.S. Park, D.H. Kim, Design of bulk metallic glasses with high glass forming ability and enhancement of plasticity in metallic glass matrix composites: A review, Metals and Materials International 11 (1) (2005) 19-27. DOI http://dx.doi.org/10.1007/BF03027480.

[3] W.L. Johnson, Bulk amorphous metal − An emerging engineering material, The Journal of The Minerals, Metals & Materials Society 54 (3) (2002) 40-43. DOI http://dx.doi.org/10.1007/BF02822619.

[4] J.F. Löffler, Bulk metallic glasses, Intermetallics 11 (6) (2003) 529-540. DOI http://dx.doi.org/10.1016/S0966-9795(03)00046-3.

[5] M. Telford, The case for bulk metallic glass, Materials Today 7 (3) (2004) 36-43. DOI http://dx.doi.org/10.1016/S1369-7021(04)00124-5.

[6] D.D. Gu, W. Meiners, K. Wissenbach, R. Poprawe, Laser additive manufacturing of metallic components: materials, processes and mechanisms, International Materials Reviews 57 (3) (2012) 133-164. DOI http://dx.doi.org/10.1179/1743280411Y.0000000014.

[7] P. Skoglund, A. Langlet, Method of producing objects containing nano metal or composite metal, U.S. Patent No. 8333922 B2.

[8] H. Sun, Microstructure evolution of bulk metallic glasses via laser processing Doctoral dissertation, The Ohio State University (2010). https://etd.ohiolink.edu/pg_10?0::NO:10:P10_ACCESSION_NUM:osu1287025216.

[9] Y.Y. Zhang, X. Lin., L.L. Wang, L. Wei, F.G. Liu, W.D. Huang, Microstructural analysis of $Zr_{55}Cu_{30}Al_{10}Ni_5$ bulk metallic glasses by laser surface remelting and laser solid forming Intermetallics 66 (2015) 22-30. DOI http://dx.doi.org/10.1016/j.intermet.2015.06.007.

[10] S. Pauly, L. Löber, R. Petters, M. Stoica, S. Scudino, U. Kühn, J. Eckert, Processing metallic glasses by selective laser melting, Materials Today 16 (1) (2013) 37-41. DOI http://dx.doi.org/10.1016/j.mattod.2013.01.018.

[11] B. Li, Z.Y. Li, J.G. Xiong, L. Xing, D. Wang, Y. Li, Laser welding of $Zr_{45}Cu_{48}A_{17}$ bulk glassy alloy, Journal of Alloys and Compounds 413 (1-2) (2006) 118-121. DOI http://dx.doi.org/10.1016/j.jallcom.2005.07.005.

[12] J.H. Kim, C. Lee, D.M. Lee, J.H. Sun, S.Y. Shin, J.C. Bae, Pulsed Nd: YAG laser welding of $Cu_{54}Ni_6Zr_{22}Ti_{18}$ bulk metallic glass, Materials Science and Engineering: A 449 (2007) 872-875. DOI http://dx.doi.org/10.1016/j.msea.2006.02.323.

[13] G. Wang, Y.J. Huang, M. Shagiev, J. Shen, Laser welding of $Ti_{40}Zr_{25}Ni_3Cu_{12}Be_{20}$ bulk metallic glass, Materials Science and Engineering: A 541 (2012) 33-37. DOI http://dx.doi.org/10.1016/j.msea.2012.01.114.

[14] F. Jiang, Z.B. Zhang, L. He, J. Sun, H. Zhang, Z.F. Zhang, The effect of primary crystallizing phases on mechanical properties of $Cu_{46}Zr_{47}Al_7$ bulk metallic glass composites, Journal of Materials Research 21 (10) (2006) 2638-2645. DOI http://dx.doi.org/10.1557/jmr.2006.0315.
[15] C.C. Hays, C.P. Kim, W.L. Johnson, Microstructure controlled shear band pattern formation and enhanced plasticity of bulk metallic glasses containing in situ formed ductile phase dendrite dispersions, Physical Review Letters 84 (13) (2000) 2901. DOI http://dx.doi.org/10.1103/PhysRevLett.84.2901.
[16] U. Kühn, J. Eckert, N. Mattern, L. Schultz, ZrNbCuNiAl bulk metallic glass matrix composites containing dendritic bcc phase precipitates, Applied Physics Letters 80 (14) (2002) 2478-2480. DOI http://dx.doi.org/10.1063/1.1467707.
[17] S.C. Glade, R. Busch, D.S. Lee, W.L. Johnson, R.K. Wunderlich, H.J. Fecht, Thermodynamics of $Cu_{47}Ti_{34}Zr_{11}Ni_8$, $Zr_{52.5}Cu_{17.9}Ni_{14.6}Al_{10}Ti_5$ and $Zr_{57}Cu_{15.4}Ni_{12.6}Al_{10}Nb_5$ bulk metallic glass forming alloys, Journal of Applied Physics 87 (10) (2000) 7242-7248. DOI http://dx.doi.org/10.1063/1.372975.
[18] J. Schroers, R. Busch, A. Masuhr, W.L. Johnson, Continuous refinement of the microstructure during crystallization of supercooled $Zr_{41}Ti_{14}Cu_{12}Ni_{10}Be_{23}$ melts, Applied Physics Letters 74 (19) (1999) 2806-2808. DOI http://dx.doi.org/10.1063/1.124020.
[19] E. Pekarskaya, J.F. Löffler, W.L. Johnson, Microstructural studies of crystallization of a Zr-based bulk metallic glass, Acta Materialia 51 (14) (2003) 4045-4057. DOI http://dx.doi.org/10.1016/S1359-6454(03)00225-8.
[20] L. Zhang, S. Pauly, M.Q. Tang, J. Eckert, H.F. Zhang, Two-phase quasi-equilibrium in β-type Ti-based bulk metallic glass composites, Scientific Reports, 6 (2016) 19235. DOI http://dx.doi.org/10.1038/srep19235.
[21] R.B. Dandliker, R.D. Conner, W.L. Johnson, Melt infiltration casting of bulk metallic-glass matrix composites, Journal of Materials Research 13 (10) (1998) 2896–290. DOI https://doi.org/10.1557/JMR.1998.0396.
[22] Y. Wu, H. Wang, Z.Y. Zhang, X.D. Hui, G.L. Chen, D. Ma, X.L. Wang, Z.P. Lu, Formation of Cu–Zr–Al bulk metallic glass composites with improved tensile properties, Acta Materialia 59 (8) 2011 2928-2936. DOI http://dx.doi.org/10.1016/j.actamat.2011.01.029.
[23] ASTM E1181-02(2015) Standard Test Methods for Characterizing Duplex Grain Sizes, ASTM International, West Conshohocken, PA, 2015. DOI https://doi.org/10.1520/E1181-02R15.
[24] Y. Shen, Y. Li, C. Chen, H.L. Tsai, 3D printing of large, complex metallic glass structures, accepted for publication in Materials and Design.
[25] W. Kurz, D.J. Fisher, Fundamentals of solidification, Trans Tech Publications 1st edition (1986) Rockport MA USA. ISBN: 0-87849-522-3
[26] J. Schroers, W.L. Johnson, History dependent crystallization of $Zr_{41}Ti_{14}Cu_{12}Ni_{10}Be_{23}$ melts, Journal of Applied Physics 88 (1) (2000) 44-48. DOI http://dx.doi.org/10.1063/1.373621.
[27] Z. Evenson, T. Schmitt, M. Nicola, I. Gallino, R. Busch, High temperature melt viscosity and fragile to strong transition in Zr–Cu–Ni–Al–Nb(Ti) and $Cu_{47}Ti_{34}Zr_{11}Ni_8$ bulk metallic glasses, Acta Materialia, 60 (12) (2012) 4712-4719. DOI http://dx.doi.org/10.1016/j.actamat.2012.05.019.

[28] A.T. Patel, H.R. Shevde, A. Pratap, Thermodynamics of $Zr_{52.5}Cu_{17.9}Ni_{14.6}Al_{10}Ti_5$ bulk metallic glass forming alloy, Journal of Thermal Analysis and Calorimetry, 107 (1) (2011) 167-170. DOI http://dx.doi.org/10.1007/s10973-011-1591-9.
[29] S. Mukherjee, Z. Zhou, J. Schroers, W.L. Johnson, W.K. Rhim, Overheating threshold and its effect on time–temperature−transformation diagrams of zirconium based bulk metallic glasses, Applied Physics Letters 84 (24) (2004) 5010-5012. DOI http://dx.doi.org/10.1063/1.1763219.
[30] J. Schroers, A. Masuhr, W.L. Johnson, R. Busch, Pronounced asymmetry in the crystallization behavior during constant heating and cooling of a bulk metallic glass-forming liquid, Physical Review B 60 (17) (1999) 11855. DOI http://dx.doi.org/10.1103/PhysRevB.60.11855.
[31] H. Kim, L. Mandelkern, Temperature dependence of the bulk crystallization rate of polymers, Journal of Polymer Science Part B: Polymer Physics 6 (4) (1968) 695-706. DOI http://dx.doi.org/10.1002/pol.1968.160060405.
[32] G. Kaltenboeck, T. Harris, K. Sun, T. Tran, G. Chang, J.P. Schramm, M.D. Demetriou, W.L. Johnson, Accessing thermoplastic processing windows in metallic glasses using rapid capacitive discharge, Scientific Reports 4 (2014) 6441. DOI http://dx.doi.org/10.1038/srep06441.